Biosensors and Bioelectronics 161 (2020) 112237

Contents lists available at ScienceDirect

Biosensors and Bioelectronics

journal homepage: http://www.elsevier.com/locate/bios

Aggregation-free optical and colorimetric detection of Hg(II) with M13 bacteriophage-templated Au nanowires

Shanmugam Manivannan, Soryun Park, Juwon Jeong, Kyuwon Kim *

Electrochemistry Laboratory for Sensors & Energy (ELSE), Incheon National University, Incheon, 22012, Republic of Korea

ARTICLE INFO

Keywords:
Au-Hg amalgam
Colorimetric sensors
Gold nanowires
Hg(II) sensors
M13 bacteriophages
Optical biosensors

ABSTRACT

An optical and colorimetric biosensor comprising gold nanowires (Au NWs) templated with genetically engineered M13 bacteriophages expressing a specific Au binding peptides tyrosine–glutamic acid–glutamic acid–glutamic acid (Y3E) is fabricated by silver nitrate and surfactant-mediated biomineralization process. The diameter of the Y3E–Au NWs is around 10 nm and an oriented growth mechanism is identified for the continuous growth of the NWs by interconnecting M13 bacteriophages. The flexible Au NWs have formed an enriched Hg(II) binding sites on its surface and the surface-coated silver nanophase functions as a receptor for more efficient Hg (II) binding. Amalgamation-based colorimetric and optical Hg(II) biosensing of Au NWs are scrutinized in the presence of wild-type M13 bacteriophage-templated Au NWs and spherical Au nanoparticles. It is demonstrated that in comparison with the spherical Au nanoparticles, Y3E–Au NWs exhibits an aggregation-free optical and colorimetric sensor for Hg(II). Mechanistic investigation for the aggregation-free sensor and the Au–Hg amalgam crystals are carried out using TEM, STEM-EDX and XPS analyses.

1. Introduction

Au NWs are attractive materials in optical sensor applications due to their noticeable structural and surface plasmon resonance (SPR) properties. As their surface to volume ratio is pointedly higher than its family of advanced materials (spheres, triangles, nanorods and so on), they have different applications in the fields of high-performance energy materials, transistors, electrocatalysts, chemical, and biological sensors. Biomolecules as a template is facile, effective, compatible with biosensor platform and device fabrication, and enables obtaining templated NWs with a high density, it is particularly imperative for an economic preparation of Au NWs. In this regard, Au NWs are amongst the best contender for understanding the SPR-based optical biosensors. By employing the Au NSs, several SPR-based mercury (II) (Hg(II)) sensors have been investigated (Chen et al., 2014; Lou et al., 2011). However, the main disadvantage of the Au NSs in Hg(II) is their poor sensitivity and aggregation, which limits its practical application as a potent Hg(II) optical sensor platform (Jin et al., 2016; Zhou et al., 2014). Therefore, we have designed an M13 bacteriophage (M13) templated Au NWs with partially deposited silver nanophase (Ag NP) for achieving high sensitivity and aggregation-free sensor performances.

Heavy metal ions discharged from natural and industry effluents have a severe impact on the environment, animal and human health even at minimum concentrations. Among the several heavy metal species, Hg is a pronoun toxic element known to humankind and its derivative, Hg(II) is one of the highly stable species and general inorganic versions of mercury pollution (Lou et al., 2011; Zhou et al., 2014). The M13 bacteriophage (M13) is a one-dimensional (1D) filamentous virus, having expressed 2700 copies of pVIII major coat proteins (Fig. 2A). The M13 can be prepared by infecting *Escherichia coli* (E-coli) followed by an amplification process. In this work, M13 engineered with Au binding peptides (M13-Y3E) templated flexible Au NWs was prepared and applied towards optical biosensing and colorimetric detection of Hg(II).

2. Experimental section

2.1. Materials and methods

Chloroauric acid ($HAuCl_4$), silver nitrate ($AgNO_3$), mercury (II) nitrate, β-cyclodextrin (β-CD), ascorbic acid (AA), cetyltrimethylammonium bromide (CTAB), $PbCl_2$, $CoCl_2.6H_2O$, $CdCl_2$, $CaCl_2.2H_2O$, $NiCl_2.6H_2O$, $ZnCl_2$, $MnCl_2.4H_2O$, $FeCl_2.6H_2O$, $FeCl_3.6H_2O$, NaCl and NaOH were obtained from Sigma-Aldrich.

* Corresponding author.
E-mail address: kyuwon_kim@inu.ac.kr (K. Kim).

https://doi.org/10.1016/j.bios.2020.112237
Received 13 February 2020; Received in revised form 15 April 2020; Accepted 23 April 2020
Available online 28 April 2020

2.2. Wild-type M13 bacteriophage (M13-wild) preparation

Wild-type M13 bacteriophage (M13-wild) was grown and purified by following standard biochemical protocols described in the literature (Seo et al., 2017; Manivannan et al., 2018). Briefly, one colony of *E. coli* XL-1 blue was grown in 3 mL of LB media to mid-log phase (*E. coli* XL-1 blue culture) and infected with 10 μL of M13-wild. The culture was incubated at 37 °C with shaking for 12 h, and then centrifuged to remove *E. coli*. The M13-wild was collected by PEG/NaCl (20% PEG and 2.5 mol/L NaCl) precipitation and reconstituted in Tris-buffered saline (10 mM). The typical yield was ~20 mg of M13-wild per litter. The final concentration was determined spectrophotometrically using an extinction coefficient of 3.84 cm^2/mg at 269 nm.

2.2.1. Y3E peptides engineered M13 bacteriophage (M13-Y3E) preparation

Attachment of Au binding peptides at the major coat protein (Gene VIII) of M13 is reported previously (Seo et al., 2017). Briefly, two primers were designed to insert Y3E into the gene VIII protein: 5′-ATATATCTGCAGNKTAYGAA-GAGGAANNKGATCCCGCAAAAGCGGCCTTTA ACTCCC-3′ (Y3E) and 5′-GGAAGCTGCAGCGAAAGACAGCATCGGAACGAGG-3′ (linearization primer). To collect M13-Y3E, the inverse polymerase chain reaction (PCR) cloning method was performed using the above-mentioned primers. The PCR product was purified then the amplified plasmid, and phage plaques were verified by DNA sequencing. Furthermore, we have amplified the M13-Y3E for our experiments, and the methods were the same as the M13-wild as mentioned in section 2.2. Fig. 2A demonstrates the structural features of the M13-Y3E used in this study.

2.3. Preparation of Au and AuAg NPs

At first, spherical Au NPs was prepared from the previous method (Manivannan and Ramaraj, 2012) by dissolving 0.792 g of β-CD (final concentration: 7 mM) in 100 mL of DI H_2O and then 0.4 mL of 10 mM $HAuCl_4$ (final concentration: 0.00004 M) was added into it. After 2 min, 1 mL of 1 M NaOH was added to the above solution to bring the solution pH to ~10–12. Then, the reaction mixture was shaken well and heated in a water jacket apparatus at 75 °C for 1 h. Afterward, 0.000001647 M of $AgNO_3$ was added to obtain the Ag nanophase over Au NPs, like that of Y3E–Au NWs.

2.4. Preparation of Y3E–Au NWs and wild–Au NWs

Fig. 2A represents a schematic illustration for the preparation of M13-Y3E templated Y3E–Au NWs over the time frame of 0–5 hr. A 0.005 mg/mL of M13-Y3E was dispersed in 25 mL performed 0.06 M of CTAB +0.0000136 M of Au^{3+} ions mixture, obtained deep yellow color mixture was incubated at 25 °C for 3 hr under mild shaking (120 rpm). Subsequently, 150 μL of 0.1 M AA was added into a reaction mixture to facilitate the reduction process, then 1.4 μL of 0.01 M $AgNO_3$ was introduced and the reaction mixture further incubated for an hr at 25 °C. Washed with DI water for several times to remove the excess CTAB and stored in a DI water for further use. The wild–Au NSs were prepared using the same procedure by replacing M13-Y3E.

2.5. Optical biosensor and colorimetric detection of Hg(II)

The optical detection of Hg(II) using Y3E–Au NWs was performed using a Shimadzu UV2550 spectrophotometer. The absorption spectra were recorded upon the addition of fixed concentrations of Hg(II). The calculated concentrations of as prepared Y3E–Au NWs and AuAg NPs were 2.60 μg/mL and 7.85 μg/mL, respectively. To begin with, sensor-probes' optical densities (OD) values were initially adjusted to 1 by using DI H_2O before commencing each experiment. Regarding the scanning period wavelength in the spectrophotometer, the following parameters were followed; scan speed: medium and sample interval: 0.5, both the parameters were maintained constant for all sensor experiments of this study. During an optical biosensing, a microliter volume of freshly prepared Hg(II) ion solution was added to 2 mL of Y3E–Au NWs or 2 mL of AuAg NPs solution taken in a quartz cuvette, shaken well and allowed for a constant resting time of 5 min, and the optical perturbations were recorded. For selective and colorimetric sensing, the optimum level of Hg(II) was added into a Y3E–Au NWs solution containing a known concentration of other common metal ions, shaken well and allowed for 5 min to interact, then the spectra were recorded. Subsequently, fading/de-coloration of the Y3E–Au NWs solution was monitored by a naked eye.

3. Results and discussion

3.1. Morphological characterization and growth mechanism

Fig. 1 shows TEM, SEM and STEM-EDX images of spherical the AuAg NPs and Y3E–Au NWs. TEM images of the AuAg NPs (Fig. 1A–D) are demonstrating a spherical morphology with a particle size around 10 nm. For Y3E–Au NWs, final morphology is comprised of the long NWs with a length of several micrometers, as presented in the low magnification SEM images in Fig. 1E–G. Furthermore, a high magnification SEM image (Fig. 1G) is presenting an interpenetrated NWs structure. From low magnification SEM images, it can be understood that NWs morphology is more dominant and spherical Au or AuAg NPs were not seen; supporting a successful biomineralization process assisted by the M13-Y3E. To get deeper insight, TEM analysis was carried out and the results are presented in Fig. 1H–K, it can be learned that the Y3E–Au NWs were continuously grown by interconnecting as well as templating the M13-Y3E. Besides, due to a fibrillar nature; NWs were interpenetrated with each other; as a result, several junctions were created at the point of interpenetration. Those junctions (Fig. 1J and K) can involve in signal amplification of the sensor platform by encouraging the Au–Hg amalgam growth at the interface region. Also, it is found that NWs are not made up of assembled spherical Au NPs; actually, it is nucleated and has grown continuously with high surface roughness. Furthermore, Y3E–Au NWs has last long for several micrometers in length and around 10–15 nm in diameter.

It attributes that, approximately 5 nm thickness of the Au portion was templated over the M13-Y3E during nucleation and growth process. Fig. 1L–O shows the HAADF image and STEM-EDX elemental mapping analysis of the Y3E–Au NWs; Au and Ag elements distributions are confirmed and are distributed uniformly over NW's surface. The Ag^+ ions added as a growth directing agent during the synthesis step were found at the Y3E–Au NWs as Ag NP with homogeneous compositions over NWs. Hence, Au NWs reported here is an alloy Y3E–Au–Ag NWs with ~4% atomic Ag composition.

Fig. 2 represents the M13-Y3E's structural features and schematic representation of the Y3E–Au NWs preparation along with STEM-EDX analysis at a juncture of the two M13-Y3E. As can be seen from the HAADF image (Fig. 2B); Au templating has occurred continuously and it is highly crystalline, especially at the junction (Fig. 2D and E), no discontinuity or mere attachment are seen. These observations concretes that during the nucleation and growth step, M13-Y3E was brought close to each other subsequently, Au templating had occurred. It is noteworthy to mention that identifying the continuous growth of Au NWs supported by either head to head or head to tail interaction is very difficult. Furthermore, specific nucleation of Au precursors and continuous growth into NWs were facilitated by the Y3E functionalization on M13. To prove Y3E's contribution, a controlled experiment was carried out by employing M13-wild instead of M13-Y3E and the obtained M13-wild-Au NS's SEM analysis is given in Fig. S1. As can be seen, spherical NPs are the dominant structures and there are few discontinuously grown NWs too. This observation confirms that the Y3E functionalization on M13 is mandatory for nucleation and continuous growth of Au NWs. A significant challenge of this study is designing a synthetic

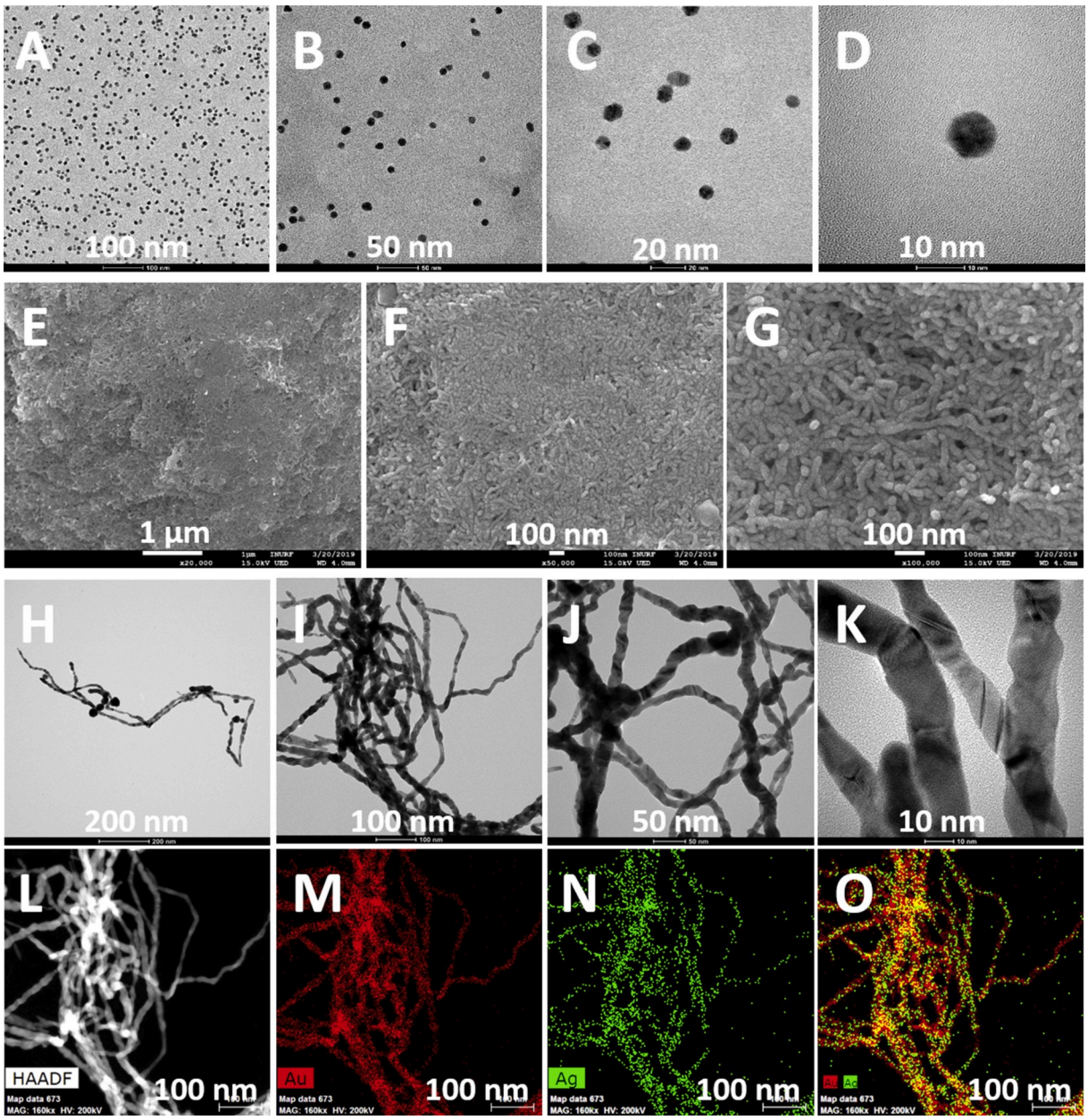

Fig. 1. **(A–D)** TEM images of Au NPs at different magnifications. **(E–G)** SEM images, **(H–K)** TEM images, **(L)** STEM-HAADF image and **(M–O)** STEM-EDX elemental mapping analyses of Y3E–Au NWs.

method that can generate uniform NWs without interference such as discontinuity and spherical particle growth. Furthermore, applications of spherical Au NPs have been limited by the aggregation/agglomeration during the sensor studies. In this regard, exploiting unique features and functionalities of Au NWs are generally limited by the non-uniformity, inhomogeneous with spherical NPs, and uncontrollable variations in diameter. To overcome these limitations, the present strategy to prepare Y3E–Au NWs is facile and carried out in an aqueous phase as well as at room temperature. Also, the present methodology has benefits such as (i) a genetically engineered M13-Y3E acts as a template in a biomineralization process that produces an excellent conversion efficiency of Au precursors into Au NWs; (ii) introducing CTAB molecules into the present bio-inorganic composite refrains the final morphology of Au NWs which, makes this methodology's suitability to control the length and diameter of Au NWs as well as loading amount. (iii) Prepared Au NWs can be used as a bio-templated core, to nucleate and deposit other noble metals such as platinum (Pt) and Ag as a shell, thereby generalized synthetic routes can be developed. Previously Belcher and co-workers (Lee et al., 2012) have used the M13 phage clone, named p8#9, displays 2700 copies of the peptide sequence Val-Ser-Gly-Ser-Ser-Pro-Asp-Ser (VSGSSPDS) on the N-terminus of p8 for preparing Au NWs. Using the p8#9 clone, Au NWs with an average diameter of 30 nm have been obtained. On the contrary, in this study an average diameter of 15 nm is obtained by using the Y3E clone. It is almost 50% less than the previous report by Belcher et al. which makes the present methodology more advantageous in terms of decreasing the loading amount, increased active surface area, cost-effective, more flexible and improved interpenetration thus more no. of active plasmonic junctions were created.

3.2. Aggregation-free optical biosensor platform for Hg(II)

Surface plasmon resonance (SPR) is a pronoun optical property of the noble metal NPs and it is defined as "collective oscillation of the

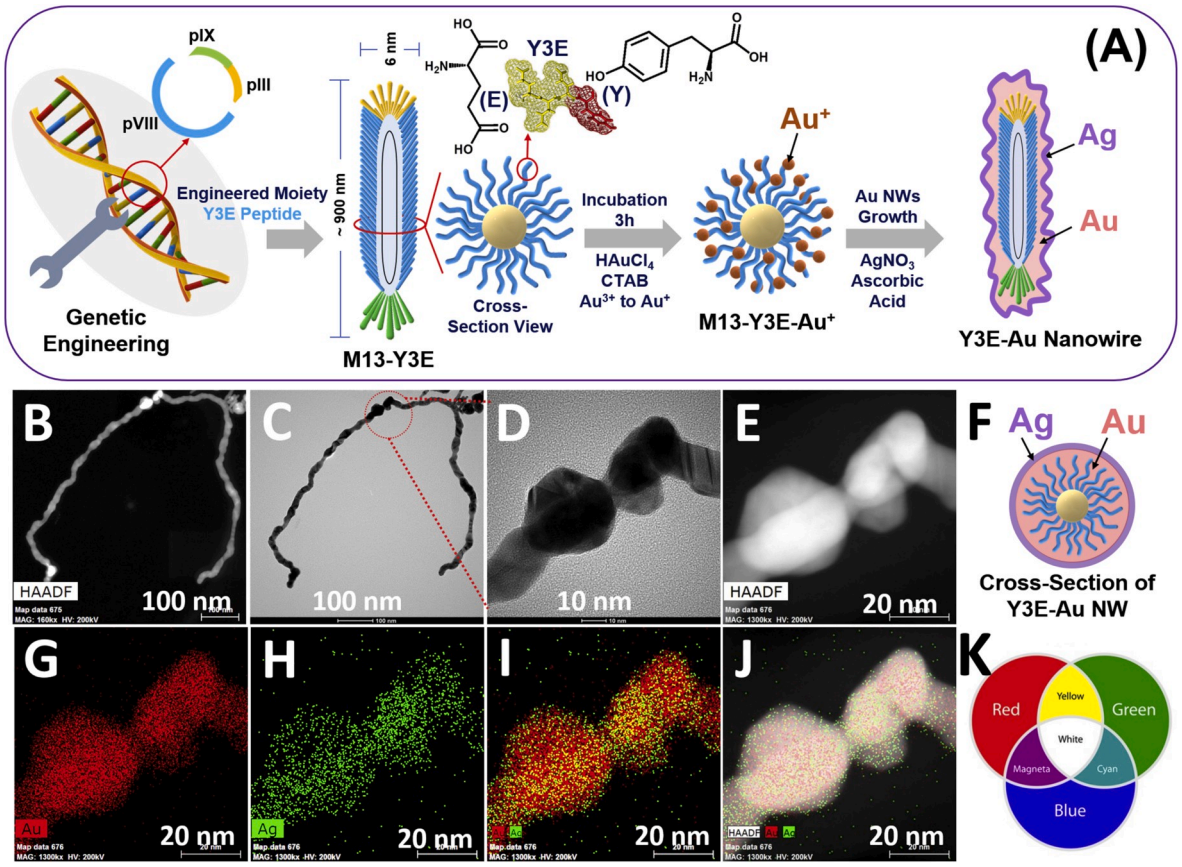

Fig. 2. Preparation of Y3E–Au NWs. (A) Schematic representation of the M13–Y3E virus's structure with specific Au binding peptides (Y3E; Y: Tyrosine and E: Glutamic acid) on the major coat protein and preparation of Y3E–Au NWs from M13–Y3E virus: Y3E–Au NWs were obtained from the specific interaction during incubation between the Au^{3+} ions and Y3E, in the presence of CTAB as mentioned. Addition of $AgNO_3$ followed by the addition of ascorbic acid resulted in Au^{+} reduction as well as partial Ag NPs deposition on the surface of M13–Y3E viruses. (F) The cross-sectional view denotes a basic multi-layer structure of the NW. (**B** and **E**) STEM-HAADF and (**C** and **D**)TEM images of the Y3E–Au NWs show the oriented growth attachment in making the continuous NW. (**G-J**) STEM-EDX analysis on the Y3E–Au NWs clearly showed the presence of individual element; Au: red and Ag: green. (**K**) Pictorial demonstration of the mixture of light colors (https://marketingaccesspass.com/what-color-does-red-and-green-make/). (For interpretation of the references to color in this figure legend, the reader is referred to the Web version of this article.)

conduction band electrons" and the metal NPs in the size range of 5–100 nm do exhibit one or more strong absorption peaks in the visible to near IR region, referred as an SPR band (Mahmoudpour et al., 2019; Zeng et al., 2019; Zhao et al., 2019). Such SPR band position is purely dependent on the size, shape and surrounding environment of the NSs. Transverse and longitudinal plasmon resonance modes are characteristic of noble metal nanorods and NWs. In which, longitudinal plasmon resonance mode arises while an electric field polarized along the main axis (z-direction) of the nanorod or nanowire. Hence, change in nanowire length, pending and interpenetration can result in a transformation in energy and strength of a longitudinal plasmon resonance mode. On the contrary, the transverse mode is a result of the electric field polarized perpendicular to a main axis (x-direction) of NPs or nanorod or nanowire. In general, the former tends to redshift in wavelength concerning aspect ratio whereas, later does not get much effect concerning an increasing aspect ratio. Fig. 3A represents the SPR absorption spectra of Au NPs and Y3E–Au NWs, as can be seen; Au NPs (Fig. 3A(a)) has exhibited a strong transverse absorption band at 512 nm. In comparison with the spherical Au NP's SPR spectrum, the present Au NPs spectrum has slightly blue-shifted for around 8 nm and it can be attributed to the added Ag^{+} during the synthesis step to meet a procedure similar to that of Y3E–Au NWs, since it is a control experiment. Moreover, Y3E–Au NWs has exhibited two bands (Fig. 3A(b)) centered at 534 and 714 nm and they are characteristic transverse and longitudinal modes of the NWs, respectively.

Also, the intensity of a longitudinal band is relatively weak in comparison with a transverse band and it can be attributed to the pending and interpenetration occurred with the Y3E–Au NWs as noticed in TEM image (Fig. 1J). Fig. 3A(inset) is representing a color modulation concerning NPs and NWs morphology. To assess Y3E–Au NWs ability toward sensing of Hg(II), 140 μM of Hg(II) was added into the Y3E–Au NWs solution; as can be seen, the color of the solution has immediately disappeared along with the quenching in the SPR spectrum and SPR absorption spectra recorded before and after the addition of 140 μM of Hg(II) were shown in Fig. 3B. Based on this preliminary experiment, sensor experiments were carried out for Au NPs and Y3E–Au NWs by SPR absorption-based titration with the addition of each 10 μM of Hg(II) and the results are summarized in Fig. 3C–F. SPR bands of both sensor-probes were sensitive to the added Hg(II), but the trend in quenching is completely controversial to each other as observed from Fig. 3C and E. For Au NPs (Fig. 3C), upon adding of Hg(II) until 80 μM; smaller red shit was noticed along with linear quenching, suddenly from 90 μM onwards, drastic redshift and non-linear quenching were noticed until 160 μM of Hg(II). Both decrement in quenching, as well as redshift in SPR bands, were scrutinized from a calibration plot (Fig. 3D). On the contrary, considerable redshift and non-linear quenching in the SPR band of Y3E–Au NWs was not observed (Fig. 3E and F). These strange observations learned from both sensor-probes are suggesting that; due to a flexibility of Y3E–Au NWs, random stacking between the Y3E–Au NWs were occurred and induced the multiple junctions and demonstrated an

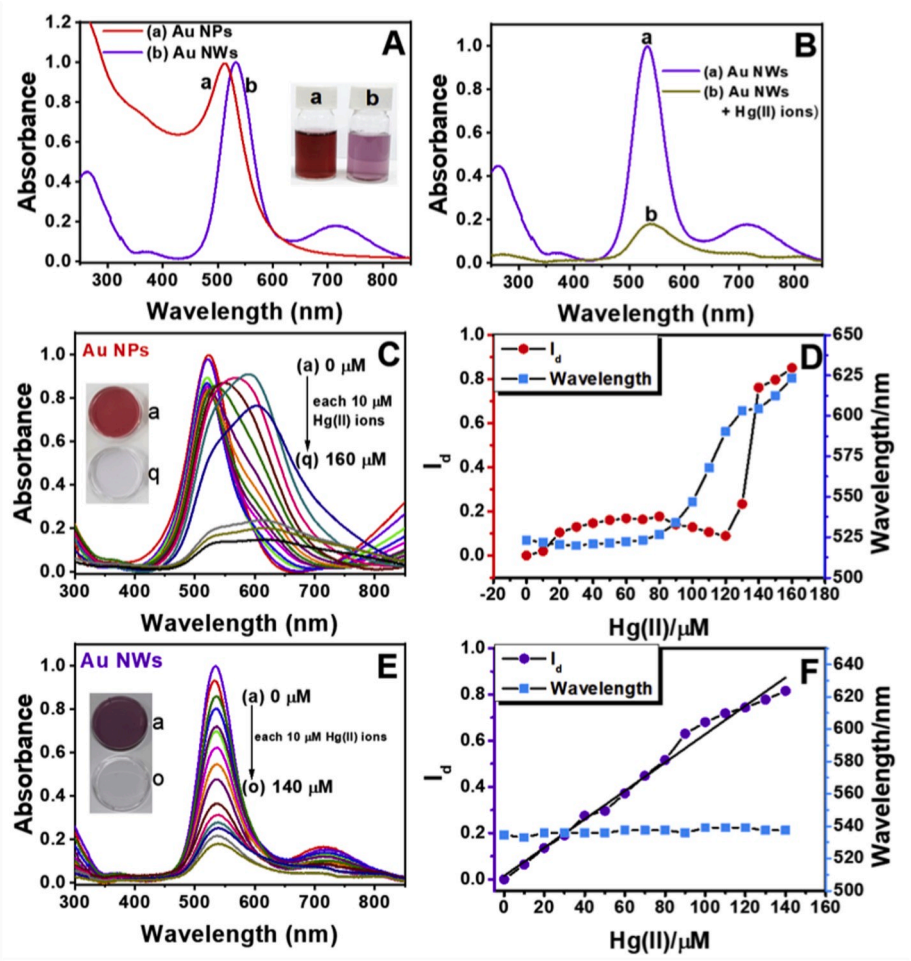

Fig. 3. (A) SPR absorption spectra of (a) Au NPs and (b) Y3E–Au NWs. (B) SPR absorption spectral changes observed for the Y3E–Au NWs (a) before and (b) after the addition of 140 μM Hg(II). Inset: A digital photographic image taken for the corresponding solutions. (C and E) SPR absorption spectral changes and (D and F) plots of changes in the absorption intensity and wavelength observed for (C and D) Au NPs and (E and F) Y3E–Au NWs upon addition of different concentrations of Hg(II).

aggregation-free sensor. Whereas Au NPs are not capable of demonstrating a wide linear range for detecting Hg(II) hence, the aggregation has occurred around 80 μM. Drastic redshift and non-linear quenching are the characteristic indications for aggregation and are not favored for developing of a sensor-probe. Moreover, partially deposited Ag NP present on Y3E–Au NWs has assisted in pre-concentrating Hg(II), thereby facilitates an active interaction between Au NWs and Hg(II) and led to an aggregation-free sensor-probe for detecting Hg(II). To measure the experimental limit of detection (LoD), Hg(II) concentration of each 1 μM was added to the Y3E–Au NWs and the calibration plot was derived (Fig. S3). The experimental LoD was estimated to be 124 nM for Y3E–Au NWs. The performance of some of the metal nanocomposites towards Hg (II) with the present Y3E–Au NWs is compared and given in Table S1.

3.3. Mechanistic investigation at the biosensor platform

It was demonstrated that the Y3E–Au NWs sensor-probe can detect a wide range of Hg(II) without any aggregation in comparison with Au NPs, hence it is mandatory to reveal the operating mechanism between Y3E–Au NWs and Hg(II) by suitable morphology and element-level investigation, hence TEM, STEM-EDX, XPS, and ICP-OES analyses were carried and are summarized in Figs. 4 and 5 and S2. Partially deposited Ag NP present on Y3E–Au NWs might lead to the two possible reactions with the added Hg(II): (i) deposition of a zero-valent Hg and (ii) growth of an amalgam between Hg and Au. From the TEM images (Fig. 4A–E), after an addition of 140 μM of Hg(II); due to the flexibility of Y3E–Au NWs, random stacking between the Y3E–Au NWs were occurred and have induced the multiple active junctions to interact with the added Hg(II); hence, NWs morphology was almost retained along with a newly grown spherical Au–Hg or Ag–Hg amalgam NPs. The STEM-EDX analysis (Fig. 4F–J) further supports the active presence of Au, Ag and Hg elements in a uniform manner throughout the Y3E–Au NWs; added Hg(II) were got reduced into its zero oxidation state (Hg (0)) and did deposit over the Y3E–Au NWs. It is speculated that, the spherical particles observed in the TEM image (Fig. 4B) might be rich in Ag–Hg amalgam formed between Ag NP and added Hg(II). On the contrary, as predicted from SPR titration of the Au NPs with the Hg (II), the aggregation has occurred as shown in Fig. 4K-M. Moreover, a close view on Figure 4M reveals that the spherical Au NPs are fused and has formed a network-like structures. Due to the high interaction between Au NPs surface (negatively charged) and Hg(II); subsequently reduced Hg (0) is got deposited over Au NPs surface and led to a growth of network-like Au–Hg amalgam structures. Corresponding STEM-EDX analysis of the Au–Hg amalgam is given in Figure 4N and O; demonstrative of corresponding elements to support a network-like structure.

Moreover, to obtain a sophisticated element level evidence, XPS analysis was carried out for Y3E–Au-Hg NWs and its core-level spectra were compared with the Y3E–Au NWs (before adding Hg(II)) and are summarized in Fig. 5. The core-level spectra of Au 4f (Fig. 5B) region of Y3E–Au NWs has showing two peaks at the binding energy values of 82.1 and 85.7 eV for Au 4f7/2 and.

Au 4f5/2, respectively suggesting the presence of Au (0) and

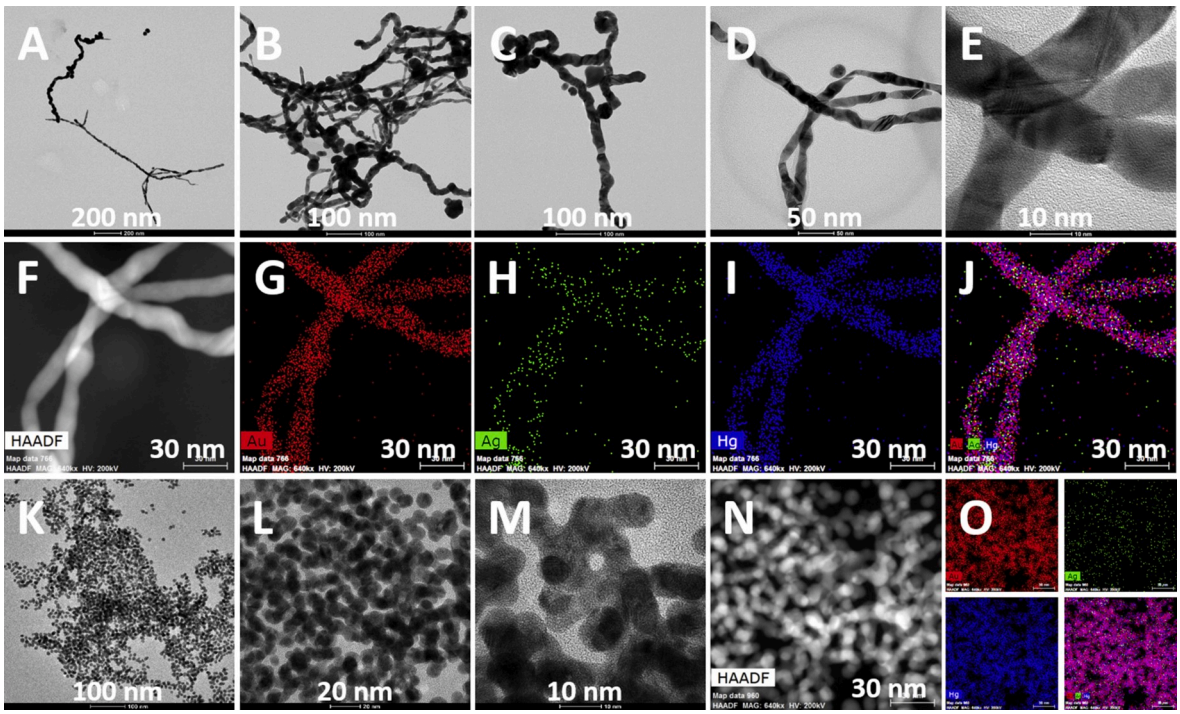

Fig. 4. (**A–E**) TEM images, (**F**) STEM-HAADF image and (**G–J**) STEM-EDX mapping analyses of the Y3E–Au-Hg NWs and (**K-M**) TEM images, (**N**) STEM-HAADF image and (**O**) STEM-EDX mapping analyses of the Au–Hg NPs.

complete reduction of the Au precursor. The core-level spectra of Ag 3 d (Fig. 5C) exhibit four peaks at 366.4, 373.6, 376.8 and 378.9 eV for Ag 3d5/2, Ag^{+} 3d5/2, Ag 3d3/2 and Ag^{+} 3d3/2, respectively suggesting the presence of both Ag (0) and Ag(I) oxidation states. On the contrary after the addition of Hg(II), two additional peaks than the Au (0) oxidation states (Fig. 5E) are deconvoluted at 84.36 and 88.1 eV for Au^{3+} 4f7/2 and Au^{3+} 4f5/2, respectively. For Ag (Fig. 5F) five additional peaks than the Ag (0) and Ag(I) oxidation states are deconvoluted at 375.2, 376.5, 377.8, 378.9 and 380.3 eV and are assigned to AgHg amalgam crystals with different Ag and Hg compositions. Also, the core-level spectra of Hg 4f (Fig. 5D) has exhibit four peaks at the binding energy values of 100.39, 101.31, 104.28 and 104.8 eV for Hg^{0} 4f7/2, Hg^{2+} 4f7/2, Hg^{0} 4f5/2, and Hg^{2+} 4f5/2, respectively. From these additional peaks of the core-level spectra of Au, Ag and Hg; it can be understood that presence of corresponding Au(III), Ag(I) and Hg (0) are obvious and are due to the formation of Au–Hg and Ag–Hg amalgams upon the addition of Hg(II) into the Y3E–Au NWs. Furthermore, core-level analysis of Hg 5p region didn't display any of the peaks for Hg

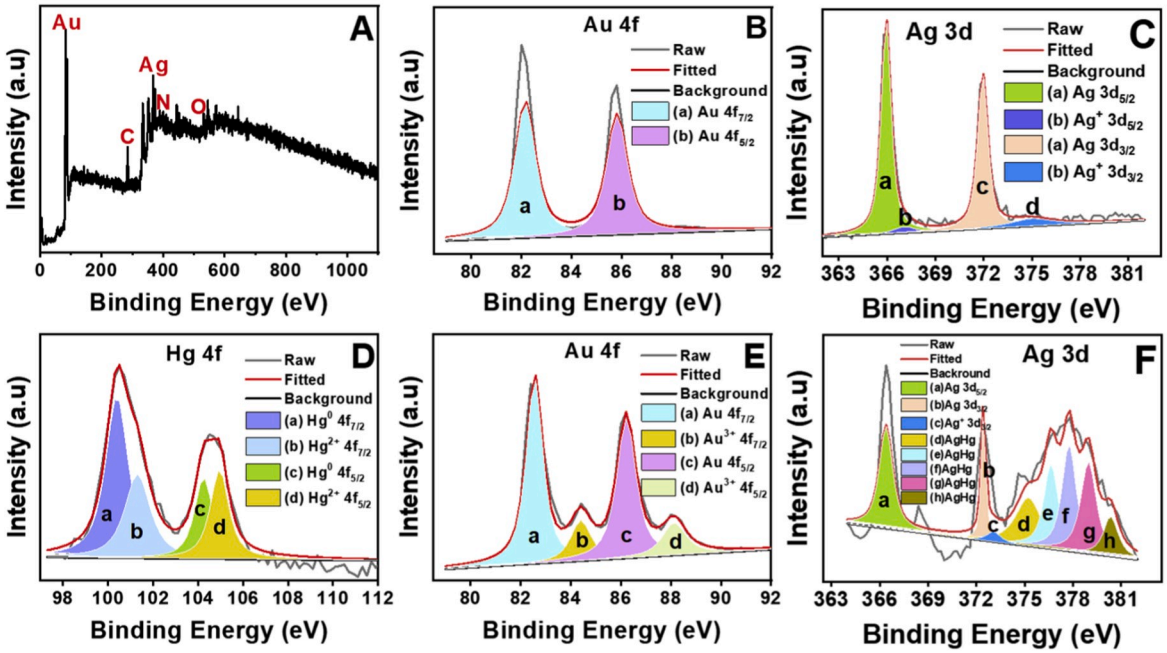

Fig. 5. XPS spectra obtained for the (**A-C**) Y3E–Au NWs and (**D-F**) Y3E–Au-Hg NWs and their corresponding (**A**) survey, (**B** and **E**) Au4f, (**C** and **F**) Ag3d, and (**D**) Hg4f regions of core-level spectra.

5p1/2 and Hg 5p3/2 and they are characteristic for the added Hg(II) (Vasimalai and John, 2013); which confirms the absence of added Hg(II) and those were consumed by the Y3E–Au NWs for the growth of an amalgam. From the ICP-MS analysis, the composition of the Au–Hg and Ag–Hg amalgam crystals were identified as 56.48%: 43.5%; $Au_{1.29}Hg_1$ and 60.48%: 39.5%; $Ag_{1.53}Hg_1$, respectively. These observations represent that Hg was present in its Hg (0) state and Au–Hg and Ag–Hg amalgam crystal's growth were apparent after the addition of Hg(II) into the Y3E–Au NWs.

3.4. Colorimetric detection and optical biosensor

Here, by taking advantage of high affinities of Au and Ag NP of the Y3E–Au NWs toward Hg(II), a very simple colorimetric sensor was developed for Hg(II) detection based on a modulation in color of Y3E–Au NWs by naked-eye as shown in Fig. 6. In comparison with the known sensors for Hg(II), the proposed method offers several important advantages including (1) simplicity of using as prepared Y3E–Au NWs as a sensor-probe without any modification and design; (2) rapid assay time and lab-friendly condition (room temperature, aqueous solution); (3) high selectivity for Hg(II) over other metal ions without any aggregation as well as any of the masking agents were not used; (4) facile and straight visualization of a final result with a color modulation; and (5) low cost due to the use of cost-effective production and amplification of M13 viruses.

Further experiments were carried out to explore selectivity of Y3E–Au NWs toward Hg(II) over commonly encountered metal ions in water. After the addition of each 500 μM of other metal ions (Na(I), Mn (II), Ca(II), Pb(II), Zn(II), Cd(II), Ni(II), Fe(II), Co(II), and Fe(III)) both spectral and color modulations were monitored. The relative SPR absorption spectral changes (Fig. 6A) were marked as shown in Fig. 6B and from a plot, it is noticed that significant quenching in the SPR absorption band was not observed upon the addition of these commonly encountered metal ions up to a concentration of 500 μM. Moreover, photograph (Fig. 6C) displaying a selectivity in terms of change in wine red color to colorless is visible to the naked eye, upon adding 150 μM of Hg(II) into the Y3E–Au NWs both in the absence and presence of common metal ions. Hence, the proposed Y3E–Au NWs sensor-probe is highly selective toward Hg(II) even in the presence of different commonly encountered metal ions. Practical suitability of the proposed Y3E–Au NWs sensor-probe toward real sample testing was assessed for the quantification of Hg(II) using tap and pond water samples by standard addition method and the results were given in Table S2. The water samples were collected from a drinking water tap and a pond in Incheon National University campus and assed. Values obtained for tap water were very close to the standard values, whereas for pond water samples, recovery was higher than the standard values.

4. Conclusions

A low-cost production of peptides engineered M13 bacteriophages in this study enables us to overcome the limitations of high cost and poor solubility of the synthetic peptides, and it is highly advantageous for the development of nanotechnology-based biosensor-probes. It was demonstrated that the Y3E–Au NWs sensor-probe; effectively pre-concentrated the added Hg(II) and induced the chemical interaction between Au NWs and Hg(II) and exhibited an aggregation-free sensing performance. Aggregation-free sensing mechanism was elucidated using TEM, STEM-HAADF, SEM-EDS and XPS analyses. An experimental LoD was measured as 124 nM. Fabricated sensor-probe has the advantage of high flexibility and random stacking between the Au NWs and they were responsible for the generated multiple active Hg(II) binding sites. These binding sites and partially deposited silver nanophase (Ag NP) over Y3E–Au NWs, have assisted in pre-concentrating the Hg(II) thereby facilitated an aggregation-free active interaction between Au NWs and Hg(II). Colorimetric and real sample analysis performances were highlighted a suitability of this biosensor-probe for on-site detection of environment polluting Hg(II) but its practical applicability might be constrained for high concentrated, turbid and non-immiscible analytes since the probe works based on UV–visible spectroscopy.

Declaration of competing interest

The authors declare that they have no known competing financial interests or personal relationships that could have appeared to influence the work reported in this paper.

CRediT authorship contribution statement

Shanmugam Manivannan: Conceptualization, Methodology,

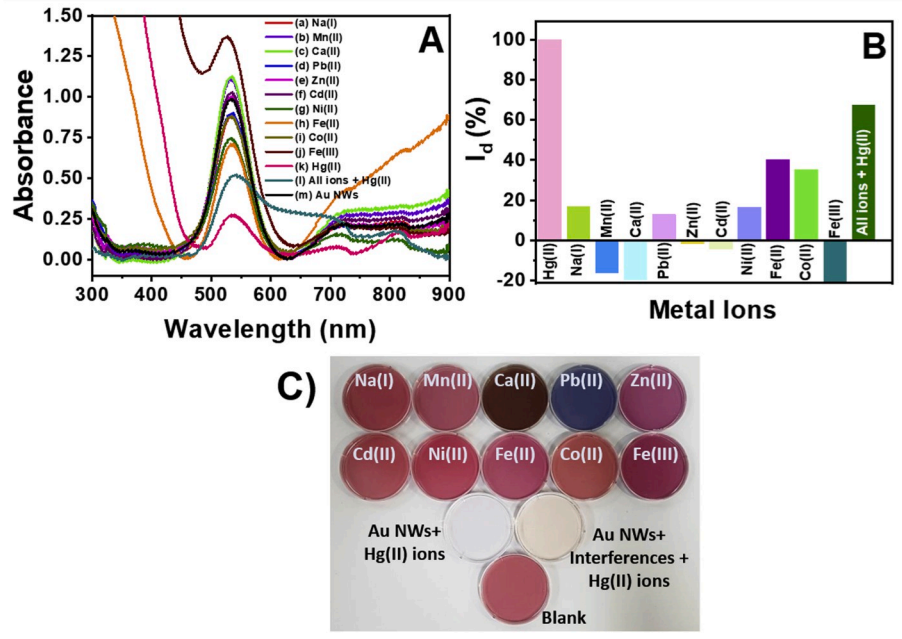

Fig. 6. (**A**) SPR spectra and (**B**) relative SPR absorption spectral changes monitored for Y3E–Au NWs upon the addition of 150 μM of Hg(II) and 500 mM of other commonly encountered metal ions, namely Na (I), Mn(II), Ca(II), Pb(II), Zn(II), Cd(II), Ni(II), Fe(II), Co(II), and Fe(III), into the individual solutions. (**C**) A photograph taken after the addition of the above-mentioned different metal ions into the individual solutions as well as in the presence of all metal ions. (**B**) A bar graph demonstrating the % of quenching to the addition of corresponding metal ions.

Writing - review & editing. **Soryun Park:** Investigation, Validation. **Juwon Jeong:** Investigation, Project administration. **Kyuwon Kim:** Supervision, Project administration, Funding acquisition.

Acknowledgments

This research was supported by Basic Science Research Program through the National Research Foundation of Korea (NRF) funded by the Ministry of Education (NRF- 2019R1A2C100478212).

Appendix A. Supplementary data

Supplementary data to this article can be found online at https://doi.org/10.1016/j.bios.2020.112237.

References

Chen, L., Li, J., Chen, L., 2014. ACS Appl. Mater. Interfaces 6 (18), 15897–15904.
Jin, W., Huang, P., Wei, G., Cao, Y., Wu, F., 2016. Sens. Actuators, B 233, 223–229.
Lee, Y., Kim, J., Yun, D.S., Nam, Y.S., Shao-Horn, Y., Belcher, A.M., 2012. Energy Environ. Sci. 5 (8), 8328–8334.
Lou, T., Chen, Z., Wang, Y., Chen, L., 2011. ACS Appl. Mater. Interfaces 3 (5), 1568–1573.
Mahmoudpour, M., Ezzati Nazhad Dolatabadi, J., Torbati, M., Pirpour Tazehkand, A., Homayouni-Rad, A., de la Guardia, M., 2019. Biosens. Bioelectron. 143 (1–14), 111603.
Manivannan, S., Ramaraj, R., 2012. J. Nanopart. Res. 14 (6), 961 (1-11).
Manivannan, S., Seo, Y., Kang, D.K., Kim, K., 2018. New J. Chem. 42 (24), 20007–20014.
Seo, Y., Manivannan, S., Kang, I., Lee, S.W., Kim, K., 2017. Biosens. Bioelectron. 94, 87–93.
Vasimalai, N., John, S.A., 2013. J. Mater. Chem. A 1 (14), 4475–4482.
Zeng, Y., Zhou, J., Wang, X., Cai, Z., Shao, Y., 2019. Biosens. Bioelectron. 145 (1–8), 1117172.
Zhao, Y., Tong, R.J., Xia, F., Peng, Y., 2019. Biosens. Bioelectron. 142 (1–12), 111505.
Zhou, Y., Dong, H., Liu, L., Li, M., Xiao, K., Xu, M., 2014. Sens. Actuators, B 196, 106–111.